Turbulent magnetohydrodynamic flow in a square duct: Comparison of zero and finite magnetic Reynolds number cases

Vinodh Bandaru,* Thomas Boeck, and Jörg Schumacher
Institut für Thermo- und Fluiddynamik, Technische Universität Ilmenau, Postfach 100565, D-98684 Ilmenau, Germany

(Received 8 November 2017; published 6 August 2018)

Three-dimensional turbulent magnetohydrodynamic flow in a duct with a square cross section and insulating walls is investigated by direct numerical simulations. The flow evolves in the presence of a uniform vertical magnetic field and is driven by an applied mean pressure gradient. A boundary element technique is applied to treat the magnetic field boundary conditions at the walls consistently. Our primary focus is on the large- and small-scale characteristics of turbulence in the regime of moderate magnetic Reynolds numbers up to $\mathrm{Rm} \sim 10^2$ and a comparison of the simulations with the quasistatic limit at $\mathrm{Rm} = 0$. The present simulations demonstrate that differences to the quasistatic case arise for the accessible magnetic Prandtl number $\mathrm{Pm} \sim 10^{-2}$ and different Hartmann numbers up to $\mathrm{Ha} = 43.5$. Hartmann and Shercliff layers at the duct walls are affected differently when a dynamical coupling to secondary magnetic fields is present. This becomes manifest by the comparison of the mean streamwise velocity profiles as well as the skin friction coefficients. While large-scale properties change only moderately, the impact on small-scale statistics is much stronger as quantified by an analysis of local anisotropy based on velocity derivatives. The small-scale anisotropy is found to increase at moderate Rm. These differences can be attributed to the additional physical phenomena which are present when secondary magnetic fields evolve, such as the expulsion of magnetic flux in the bulk of the duct or the presence of turbulent electromotive forces.

DOI: 10.1103/PhysRevFluids.3.083701

I. INTRODUCTION

Flows of electrically conducting fluids that interact with an external or self-generated magnetic field are termed magnetohydrodynamic (MHD) flows. They are of fundamental importance in most astrophysical phenomena and have their relevance in several industrial applications [1,2]. On the technological scale, magnetic fields are often applied to manipulate conducting flows, for example, in continuous casting of steel and aluminium [1], Czochralski crystal growth [3], and electromagnetic pumping of liquid metals [4]. One of the dimensionless parameters that characterize these flows is the magnetic Reynolds number Rm, which is given by the ratio of the magnetic diffusion timescale to the advection timescale. It is defined as

$$\mathrm{Rm} = \frac{t_{\mathrm{diff}}}{t_{\mathrm{adv}}} = \frac{L^2/\lambda}{L/U} = \frac{UL}{\lambda}, \tag{1}$$

where L and U represent the characteristic length and velocity scales in the flow and $\lambda = (\mu_0\sigma)^{-1}$ is the magnetic diffusivity. Here, μ_0 represents the magnetic permeability of free space and σ denotes

*Present address: Max-Planck-Institute for Plasma Physics, D-85748 Garching, Germany; vkb@ipp.mpg.de

the electrical conductivity of the fluid. The magnetic Reynolds number is the magnetic analog to the hydrodynamic Reynolds number which relates viscous diffusion to advection timescale

$$\mathrm{Re} = \frac{t_{\mathrm{vis}}}{t_{\mathrm{adv}}} = \frac{L^2/\nu}{L/U} = \frac{UL}{\nu}, \tag{2}$$

with ν being the kinematic viscosity of the fluid. Kinematic viscosity and magnetic diffusivity can be related through a third dimensionless number, the magnetic Prandtl number

$$\mathrm{Pm} = \frac{\nu}{\lambda} = \frac{\mathrm{Rm}}{\mathrm{Re}}. \tag{3}$$

In MHD flows with $\mathrm{Rm} \ll 1$, the secondary magnetic field which is generated by eddy currents, is often negligible. As a consequence, although the magnetic field influences the evolution of the turbulent velocity field through the Lorentz force density in the momentum balance, the magnetic field remains basically unchanged. This so-called *quasistatic* limit applies in particular to several technological applications of MHD turbulence for which the working fluid is a liquid metal. Early MHD laboratory experiments of Hartmann *et al.* [5] and Murgatroyd [6] in liquid mercury belong to this limit. These experiments focused on the impact of the magnetic field on the skin friction (or pressure drop). Later experiments such as those by Brouillette *et al.* [7] and Reed *et al.* [8] aimed at a deeper understanding of the transition to turbulence in the presence of a prescribed strong external magnetic field and the impact on Reynolds stresses and turbulent fluctuations.

Analytical solutions of laminar MHD shear flows have been obtained by Shercliff [9] for electrically insulated walls, Williams [10], and later Hunt [11] for electrically conducting walls. More recent studies such as direct numerical simulations (DNS) of Kobayashi [12], Shatrov *et al.* [13], and Krasnov *et al.* [14] focused on the statistical analysis of MHD turbulence in rectangular duct flows. Liquid metals are high mass density fluids and in addition, although they are good conductors of electric currents, they have very low viscosity such that resistive diffusion dominates viscous diffusion by several orders of magnitude [15]. Thus typical values of the magnetic Prandtl number are $\mathrm{Pm} \sim 10^{-5}$ and, consequently, the flow Reynolds numbers have to be as high as $\mathrm{Re} \gtrsim 10^5$ to obtain $\mathrm{Rm} \gtrsim 1$ [see Eq. (3)]. This will be the case in some of the technological applications, so that the validity of the quasistatic approximation and the differences to a full magnetohydrodynamic treatment in the same flow setup suggest a closer inspection and detailed comparison of finite-Rm with quasistatic simulations. This sets the stage for the present study.

Here, we study a simple turbulent magnetohydrodynamic shear flow at a finite $\mathrm{Rm} > 0$ by means of three-dimensional DNS and compare the statistics with the quasistatic approximation of the same flow at $\mathrm{Rm} = 0$. We take a fundamental configuration, the Hartmann-like flow [5] (sometimes also referred to as Shercliff flow) in a straight duct with a square cross section in the presence of a strong, uniform magnetic field $\boldsymbol{B}_0$. The configuration is sketched in Fig. 1. Two types of boundary layers are formed in the vicinity of the duct walls. Hartmann layers (HL) are generated at the walls normal to $\boldsymbol{B}_0$ and Shercliff layers (SL) are at the walls parallel to $\boldsymbol{B}_0$ [5,9].

We will investigate the impact of the coupling between velocity and magnetic fields on large-scale turbulence properties such as mean profiles of velocity and magnetic field, turbulent fluctuations, and drag coefficients. Our analysis also includes physical phenomena such as magnetic flux expulsion in the bulk [16] which are absent in the quasistatic limit. The explusion of magnetic flux has been analyzed recently in a two-dimensional turbulent MHD channel flow [17]. Furthermore, we investigate the impact of the dynamics of the magnetic field on the small-scale statistics. Both types of boundary layers, HL and SL, have different properties and the turbulent flow as a whole becomes anisotropic. This is quantified by local isotropy measures which are based on velocity derivatives.

The following point should be kept in mind. Flows at realistic magnetic Prandtl numbers *and* moderate magnetic Reynolds numbers are still inaccessible to DNS studies since at least six orders of magnitude in scales have to be fully resolved. Therefore, we will artificially increase the magnetic Prandtl number to $\mathrm{Pm} \sim 10^{-2}$, which will be in line with an increase of the magnetic Reynolds number to $\mathrm{Rm} \sim 10^2$. This allows us to obtain an operating point for our comparison of the differences

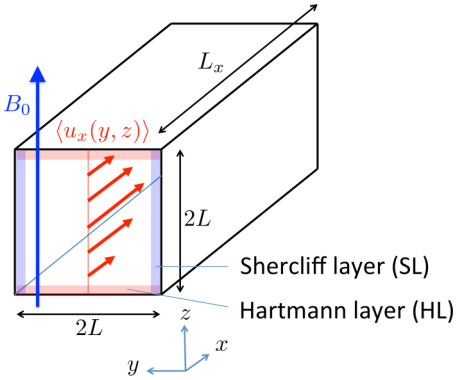

FIG. 1. Schematic drawing of the MHD duct flow configuration, with a uniform imposed vertical magnetic field, $\boldsymbol{B}_0 = B_0\boldsymbol{e}_z$. Also sketched are the Hartmann (HL) and Shercliff (SL) layers, which are formed at the field-normal and side walls of the square duct respectively. In dimensionless units, $y \in [-1, 1]$ and $z \in [-1, 1]$.

between the quasistatic limit and the full magnetohydrodynamic cases in a DNS setting. We will come back to this point in our final discussion of the results. One reason why DNS in an MHD duct flow has a limited range of accessible parameters is the more comprehensive treatment of the boundary conditions for the magnetic field in this geometry. In a nutshell, one has to solve the Maxwell equations outside the flow domain and assure continuity of magnetic field lines when they penetrate the duct. As shown in Ref. [18], this leads to the application of a boundary element technique. The DNS in that work was limited to $\mathrm{Rm} \leqslant 100$ and $\mathrm{Re} \leqslant 5000$. Here, we will extend our previous study to higher magnetic and hydrodynamic Reynolds numbers.

The outline of the paper is as follows. We first describe the governing physical model along with some details of the computational procedure in Sec. II. Results of the large-scale statistics are given in Sec. III. Here the velocity field structure, the magnetic flux expulsion, and friction coefficients will be investigated. Section IV is dedicated to the small-scale statistics. This is followed by a summary and a brief outlook in Sec. V.

II. EQUATIONS OF MOTION AND NUMERICAL METHOD

A. Magnetohydrodynamic equations

We consider the turbulent flow of an electrically conducting fluid (such as a liquid metal) in a straight duct of square cross section ($2L \times 2L$), driven by an applied mean pressure gradient $G < 0$ in the streamwise x direction. The flow is assumed to be incompressible with a constant mass density ρ. Upon this flow, a constant and uniform magnetic field $\boldsymbol{B}_0 = B_0\boldsymbol{e}_z$ is imposed, which is generated by external electric currents (see also Fig. 1). Motion of the fluid across the magnetic field generates eddy currents in the fluid whose density is given by $\boldsymbol{j}(\boldsymbol{x}, t)$. These currents in turn generate their own magnetic field, which will be referred to as the secondary magnetic field and denoted by $\boldsymbol{b}^s(\boldsymbol{x}, t)$. The total magnetic field is given by

$$\boldsymbol{b}(\boldsymbol{x}, t) = \boldsymbol{B}_0 + \boldsymbol{b}^s(\boldsymbol{x}, t) = B_0\boldsymbol{e}_z + \boldsymbol{b}^s(\boldsymbol{x}, t). \tag{4}$$

This total magnetic field interacts with the eddy currents $\boldsymbol{j}$ to produce a Lorentz force with a volumetric density of $\boldsymbol{j} \times \boldsymbol{b}$ on the fluid. The volume flow rate in the duct is assumed to be constant and periodic boundary conditions are applied in the streamwise direction. Thermal effects and gravitational forces are neglected throughout this study. The flow domain, i.e., duct interior, is denoted by Ω_i and the duct exterior by Ω_e. The physics of the problem is governed by the Navier-Stokes equation for the fluid velocity field $\boldsymbol{u}(\boldsymbol{x}, t)$ and the magnetic induction equation for the evolution of the magnetic field. The velocity and the magnetic field are constrained by the divergence-free

condition. Furthermore, Ampère's law describes the relation between the current density $\boldsymbol{j}$ and the magnetic field $\boldsymbol{b}$.

We choose the half channel width L as the characteristic length scale, the average streamwise velocity U as the velocity scale, and the magnitude of the imposed field B_0 as the scale for the magnetic field. In addition, the scales L/U, ρU^2, and $\sigma U B_0$ are used for time, pressure, and current density, respectively. The governing equations can be written in the dimensionless form as

$$\frac{\partial \boldsymbol{u}}{\partial t} + (\boldsymbol{u}\cdot\boldsymbol{\nabla})\boldsymbol{u} = -G\boldsymbol{e}_x - \boldsymbol{\nabla} p + \frac{1}{\mathrm{Re}}\nabla^2\boldsymbol{u} + \frac{\mathrm{Ha}^2}{\mathrm{Re}}(\boldsymbol{j}\times\boldsymbol{b}), \tag{5}$$

$$\frac{\partial \boldsymbol{b}^s}{\partial t} = \boldsymbol{\nabla}\times(\boldsymbol{u}\times\boldsymbol{b}) + \frac{1}{\mathrm{Rm}}\nabla^2\boldsymbol{b}^s, \tag{6}$$

$$\boldsymbol{\nabla}\cdot\boldsymbol{u} = 0, \tag{7}$$

$$\boldsymbol{\nabla}\cdot\boldsymbol{b} = 0, \tag{8}$$

$$\boldsymbol{j} = \frac{1}{\mathrm{Rm}}\boldsymbol{\nabla}\times\boldsymbol{b}, \tag{9}$$

where $\boldsymbol{\nabla} p$ refers to the pressure gradient induced in the flow field in addition to the imposed mean pressure gradient G. The third dimensionless parameter which appears in the momentum equation is the Hartmann number

$$\mathrm{Ha} = B_0 L\sqrt{\frac{\sigma}{\rho\nu}}. \tag{10}$$

Note that Rm and Re are related by the magnetic Prandtl number $\mathrm{Pm} = \mathrm{Rm}\,\mathrm{Re}^{-1} = \nu\lambda^{-1}$, which is purely dependent on the fluid properties. However, in this paper, we will treat Rm (instead of Pm) as the independent parameter.

B. Boundary conditions and treatment of magnetic field outside the duct

No-slip boundary conditions are assumed for the fluid flow at all walls Σ. These walls are additionally electrically insulating. Both conditions result in

$$\boldsymbol{u} = 0 \quad \text{and} \quad \boldsymbol{j}\cdot\hat{\boldsymbol{n}} = 0 \quad \text{for} \quad \boldsymbol{x}\in\Sigma, \tag{11}$$

where $\hat{\boldsymbol{n}}$ is the unit vector in the wall-normal direction. In the streamwise x direction, we apply periodic boundary conditions. In addition, the following constraint on the flow across the cross section $A_c = 2\times 2$ is applied:

$$\int_{A_c} u_x dA = 1. \tag{12}$$

The solution of Eq. (6) requires boundary conditions for the magnetic field at the duct walls Σ, which are not automatically implied by condition (11). Hence, it is necessary to consider the magnetic field in the exterior region in order to obtain the necessary boundary conditions for $\boldsymbol{b}$. The magnetic field in the exterior is curl free. Thus $\boldsymbol{b}^s$ can be represented by a magnetic scalar potential ψ which leads to $\boldsymbol{b} = \boldsymbol{B}_0 - \nabla\psi$. The resulting equation for the secondary magnetic field in the exterior is

$$\nabla^2\psi = 0 \quad \text{in} \quad \Omega_e \cup \Sigma. \tag{13}$$

Taking advantage of the periodicity in the x direction, we can use a Fourier transformation as

$$[\boldsymbol{b}^s, \psi](\boldsymbol{x}, t) = \Re\left\{\sum_{k=0}^{k=\frac{N_x}{2}-1} \left[\hat{\boldsymbol{b}}_k^s, \hat{\psi}_k\right](y, z, t)\exp(i\alpha_k x)\right\}, \tag{14}$$

which, when inserted into Eq. (13), yields a Helmholtz equation for each streamwise wave number of the exterior magnetic field,

$$\left(\nabla^2 - \alpha_k^2\right)\hat{\psi}_k = 0, \tag{15}$$

along with the definition

$$\hat{\boldsymbol{b}}_k^s(y,z,t) = \begin{pmatrix} -i\alpha_k\hat{\psi}_k \\ -\frac{\partial\hat{\psi}_k}{\partial y} \\ -\frac{\partial\hat{\psi}_k}{\partial z} \end{pmatrix}. \tag{16}$$

Here, $\alpha_k = 2\pi k/l_x$ represents the streamwise wave number, where $l_x = L_x/L$ is the length of the duct. Additionally, we introduce the following notation used in the two-dimensional Fourier space. The rectangular boundary is denoted by Γ, the coordinate along the path of this boundary is denoted by l. Furthermore, $\boldsymbol{r} = y\boldsymbol{e}_y + z\boldsymbol{e}_z$ denotes the position vector in the yz plane and n refers to the direction that is outward normal to Γ. Very far away from the duct walls, the magnetic field satisfies the far-field condition $\hat{\boldsymbol{b}}_k^s \to 0$ and $\hat{\psi}_k \to 0$, respectively. Then the solution can be expressed as a boundary integral equation for $\hat{\psi}_k$ at the rectangular boundary as

$$\beta(\boldsymbol{r}')\hat{\psi}_k(\boldsymbol{r}') = \text{P.V.}\oint_\Gamma \left[G_k(\boldsymbol{r}',\boldsymbol{r})\hat{b}_{nk}^s(\boldsymbol{r}) + \hat{\psi}_k(\boldsymbol{r})\frac{\partial G_k(\boldsymbol{r}',\boldsymbol{r})}{\partial n}\right] dl(\boldsymbol{r}), \tag{17}$$

where $\hat{b}_{nk}^s(\boldsymbol{r}) = -\partial_n\hat{\psi}_k(\boldsymbol{r})$ and $\beta(\boldsymbol{r}')$ is a constant that depends on the location of the pole $\boldsymbol{r}'$ on the boundary contour Γ. One has $\beta(\boldsymbol{r}') = 3/4$ when $\boldsymbol{r}'$ is a corner point of Γ and $\beta(\boldsymbol{r}') = 1/2$ otherwise (see Bandaru *et al.* [18], Iskakov *et al.* [19] for further details). G_k represents the Green's function of the Helmholtz operator and is given by

$$G_k(\boldsymbol{r}',\boldsymbol{r}) = \frac{1}{2\pi}K_0(\alpha_k|\boldsymbol{r}'-\boldsymbol{r}|), \tag{18}$$

with K_0 being the MacDonald function which corresponds to the complex Hankel function of order zero, H_0 [20]. It can be seen that the evaluation of both, $\beta(\boldsymbol{r}')$ and $G_k(\boldsymbol{r}',\boldsymbol{r})$, requires the knowledge of only the geometry of the duct. Hence they are known *a priori*. Equations (16) and (17) together constitute the nonlocal boundary conditions that are necessary for the solution of (6) and hence the need to explicitly solve for the magnetic field in the duct exterior can be avoided.

In this paper, results for moderate Rm are compared with those for the *quasistatic* limit $\text{Rm} \to 0$. For the latter case $\boldsymbol{b}^s$ is neglected and thus $\boldsymbol{b} = \boldsymbol{B}_0$. The electric field is expressed as the gradient of a scalar potential ϕ and consequently Ohm's law becomes $\boldsymbol{j} = -\nabla\phi + \boldsymbol{u}\times\boldsymbol{B}_0$. The scalar potential ϕ is obtained from the Poisson equation

$$\nabla^2\phi = \nabla\cdot(\boldsymbol{u}\times\boldsymbol{B}_0), \tag{19}$$

with Neumann boundary conditions $\partial_n\phi = 0$ at Σ. This equation sustains a divergence-free current density field and is solved instead of the induction equation (see also Tympel *et al.* [21] for further details).

C. Numerical method and direct numerical simulations

The duct domain ($l_x\times2\times2$) is discretized into a rectangular Cartesian grid and the variables are approximated at the grid points (collocated grid arrangement). A uniform grid is used in the x direction, whereas grid stretching is applied in the y and z directions to resolve the thin boundary layers near the walls. The governing equations are solved by a second-order finite-difference scheme with explicit time stepping except for the integral equation (17), which is solved using a boundary element method [18]. We provide here a brief note on the coupling of the magnetic induction equation (6) with the boundary conditions. First, it must be noted that across the boundary Σ, all the three components of the magnetic field are continuous whereas only the tangential components

TABLE I. Parameters for the DNS. All runs are performed on a domain size of $2\pi \times 2 \times 2$. The magnetic Reynolds number Rm, the Reynolds number Re, the Hartmann number Ha, the magnetic interaction parameter (or Stuart number) $N = \mathrm{Ha}^2/\mathrm{Re}$, the magnetic Prandtl number Pm, as well as the number of grid points in the three space directions are listed. For Run 5, $\Delta x^+ = 8.9$ and $\Delta y^+_{\mathrm{min}} = \Delta z^+_{\mathrm{min}} = 1.1$ in inner viscous units taken with respect to the wall shear stress at the Shercliff layers.

	Rm	Re	Ha	N	Pm	N_x	N_y	N_z
Run 0		14 500	0	0		512	192	192
Run 1	0	14 500	29	0.06	0.0	512	192	192
Run 2	400	14 500	29	0.06	2.8×10^{-2}	512	192	192
Run 3	0	14 500	43.5	0.13	0.0	512	192	192
Run 4	200	14 500	43.5	0.13	1.4×10^{-2}	512	192	192
Run 5	400	14 500	43.5	0.13	2.8×10^{-2}	512	192	192

of the electric field are continuous (see Ref. [22]). Because of this, Eq. (6) is valid on Σ only for the component of $\boldsymbol{b}^s$ normal to the boundary and hence is used to compute b^s_n at each time step. The b^s_n so computed is used in the Fourier space (as $\hat{b}^s_{nk}$) to compute $\hat{\psi}_k$ through Eq. (17), which is in turn used to compute the two tangential components of the magnetic field through Eq. (16). This procedure automatically ensures that the wall-normal component of $\boldsymbol{j}$ vanishes [Eq. (11)].

Table I summarizes the essential parameters of our series of five direct numerical simulations (DNS). A streamwise length of $l_x = 2\pi$ is found to be sufficient for a complete decay of the spatial correlations of the turbulent velocity fluctuations. Furthermore, a series of grid sensitivity studies indicated no significant differences when the streamwise and cross-stream resolutions were enhanced (see the Appendix). The simulation runs are chosen at a moderate Reynolds number $\mathrm{Re} = 14500$ along with two different Hartmann numbers $\mathrm{Ha} = 29$ and $\mathrm{Ha} = 43.5$. These parameters were also used in a large-eddy simulation study by Kobayashi [12] at $\mathrm{Rm} = 0$ and correspond to a fully turbulent regime and a partly turbulent regime respectively for the two Hartmann numbers.

It is worthwhile to note that the simulations with $\mathrm{Rm} > 0$ impose a significant computational overhead. The computational cost per time step for $\mathrm{Rm} > 0$ increased only by a factor of about 1.6 as compared to the quasistatic simulation. However, the use of explicit time stepping necessitates a significantly smaller time step for $\mathrm{Rm} \sim 10^2$. Additionally, as will be apparent in the next section, convergence of statistics for $\mathrm{Rm} > 0$ requires a much longer runtime, leading to an overall increase in computational cost. A total of about 1.8 million core hours were necessary for the moderate Rm simulations presented here.

III. LARGE-SCALE STATISTICS

A. Temporal variation of velocity and magnetic fields

The first step in the comparison is an investigation of the large-scale structure of velocity and magnetic fields. Figure 2 displays the evolution of the kinetic energy, which is obtained as the mean square of fluctuations about the streamwise average, the rescaled total enstrophy and the rescaled variance of the secondary magnetic field $\boldsymbol{b}^s$ with respect to time. The rescaling is chosen such that these quantities will be directly comparable as we will see later in the discussion of the energy balance. Runs 1, 2, 3, and 5 are shown. The quantities are defined as

$$E_{\mathrm{kin}}(t) = \tfrac{1}{2}\langle(\boldsymbol{u} - \langle\boldsymbol{u}\rangle_x)^2\rangle_V, \tag{20}$$

$$E_\Omega(t) = \frac{1}{2\mathrm{Re}}\langle\boldsymbol{\omega}^2\rangle_V, \tag{21}$$

$$E_b(t) = \frac{N}{2\mathrm{Rm}}\langle(\boldsymbol{b} - \boldsymbol{B}_0)^2\rangle_V = \frac{N}{2\mathrm{Rm}}\langle(\boldsymbol{b}^s)^2\rangle_V, \tag{22}$$

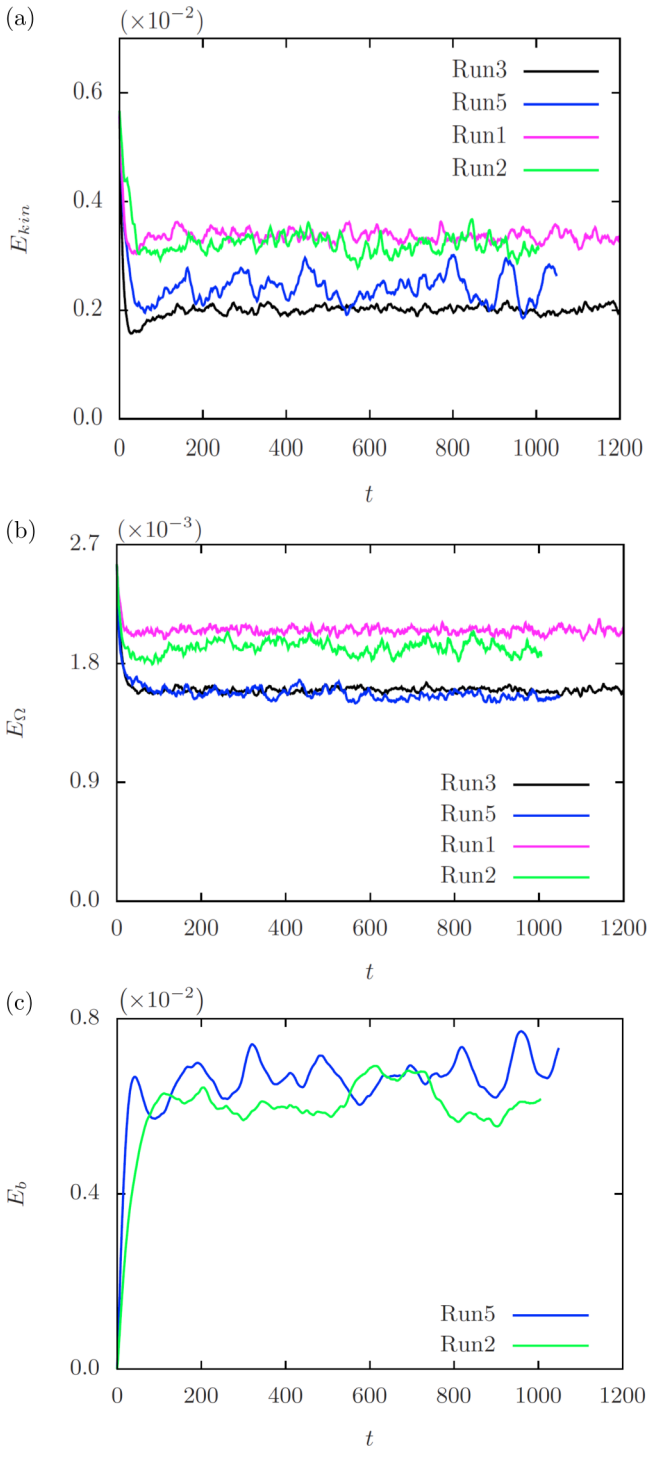

FIG. 2. Evolution of volume-averaged quantities vs time. Data for runs 1, 2, 3, and 5 are shown. (a) Kinetic energy of fluctuations. (b) Rescaled total enstrophy. (c) Energy of the secondary magnetic field $\boldsymbol{b}^s$. The subscript V indicates averaging over the whole duct. Quantities are given in (20)–(22). The hydrodynamic Reynolds number is $\mathrm{Re} = 14\,500$ in all cases.

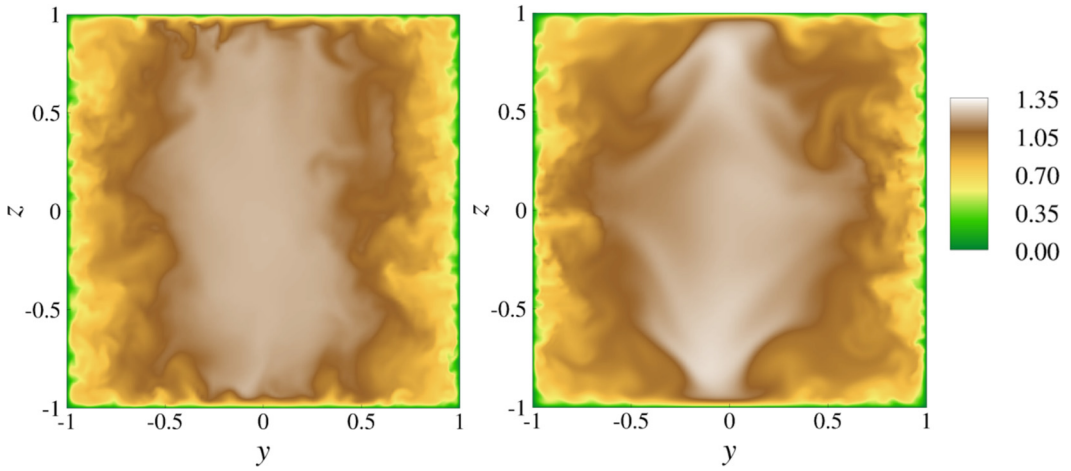

FIG. 3. Instantaneous contours of the streamwise velocity $u_x(x_0, y, z, t_0)$ at duct cross section $x_0 = \pi$. Left: run 3 at Rm = 0. Right: run 5 at Rm = 400. The contour range for both panels is indicated by the color bar to the right. Hartmann number Ha = 43.5.

where $\langle\cdot\rangle_V$ is a duct volume average, $\langle\cdot\rangle_x$ an average in streamwise direction, and $\boldsymbol{\omega} = \boldsymbol{\nabla} \times \boldsymbol{u}$. After an initial period, all runs are relaxed into a statistically stationary state which is used for the statistical analysis.

One expects that the flow at Rm = 400 shows significant differences from the flow at Rm = 0. However, it turns out that the differences for both Hartmann numbers remain small. The flow at moderate Rm is seen to settle to a slightly higher level of fluctuation kinetic energy $E_{\rm kin}$ in comparison to the quasistatic case, whereas the total enstrophy E_Ω remains almost the same. The energy in the secondary magnetic field [see Fig. 2(c)] is observed to be comparable to the fluctuation kinetic energy and hence much smaller as compared to the kinetic energy of the mean flow. The small effect of the magnetic field on the fluid motion is due to the small values of the interaction parameter N.

One distinctive feature of the statistically steady state at moderate Rm is the large temporal variation in the volume-averaged quantities occurring on a slower time scale as compared to the flow at Rm = 0. This can be seen clearly in Fig. 2(a) and confirms a similar observation made in our earlier preliminary study conducted at Re = 5000 and Ha = 15 (see Ref. [18]). Though the exact reason for such behavior is unclear, such variations may possibly be caused by the propagation of Alfvèn waves in the magnetohydrodynamic flow. These linear waves have a timescale t_A and the ratio

$$\frac{t_A}{t_{\rm adv}} = \frac{U}{v_A} = \sqrt{\frac{\rm RmRe}{\rm Ha}} = 55.4 \tag{23}$$

is much larger than unity in the present cases. Here, the Alfvèn velocity is defined as $v_A = B_0/\sqrt{\rho\mu_0}$.

We now turn to the instantaneous distributions of the velocity and magnetic fields. Figure 3 shows the comparison of the instantaneous axial velocity distribution in the middle cross section ($x = \pi$) at Ha = 43.5. It is interesting to observe that the flow at Rm = 400 (right) shows a significantly different structure in the core region of the cross section. This corresponds to the existence of large-scale turbulence in the core region at Rm = 400 in contrast to an almost laminar state at Rm = 0 (left). The effect of the moderate Rm on the boundary layers, however, is not immediately apparent from this picture. The corresponding magnetic field lines for run 5 are shown in Fig. 4 at the same instant. One can see that the field lines are stretched significantly in the direction of the mean flow, particularly in the core region. A maximum axial magnetic field amplitude of $b_x \approx 12$ develops here, with the maximum close to the Hartmann walls but not inside the boundary layers.

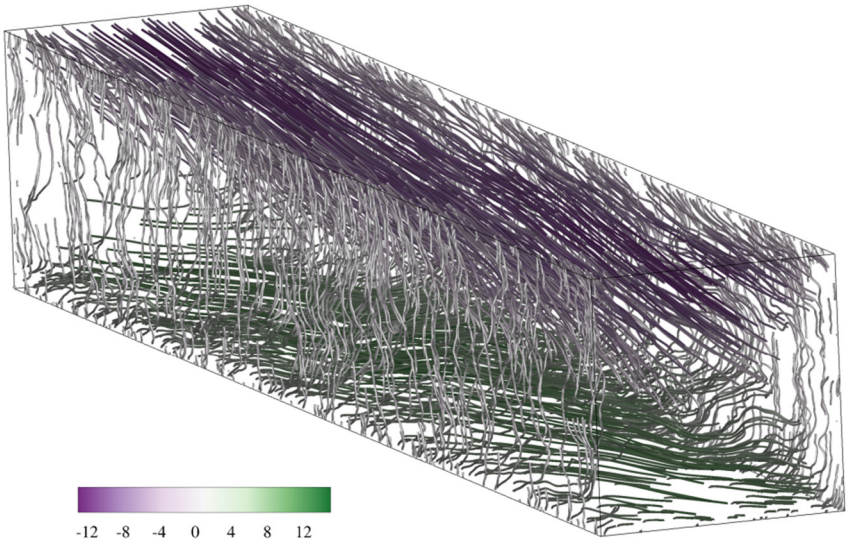

FIG. 4. Instantaneous magnetic field line plot at Rm = 400 and Ha = 43.5 for run 5 taken at the same time as in the right panel of Fig. 3. The contour coloring represents the magnitude of the streamwise magnetic field component b_x. The mean flow is from the upper left to the lower right.

Furthermore, the magnetic field also displays a significant amount of turbulence due to the fact that Pm in our case is still fairly large.

B. Mean magnetic field and flux expulsion

Mean quantities refer to fields that are averaged with respect to time *and* streamwise (x) direction in this and the subsequent subsection. They are denoted by $\langle\cdot\rangle_{x,t}$. Figure 5 (left) shows the distribution of mean axial magnetic field $\langle b_x\rangle_{x,t}$ in the duct cross section for Rm = 400. It can be seen that the resulting field is an order of magnitude larger than the imposed magnetic field $B_0\boldsymbol{e}_z$, with a change

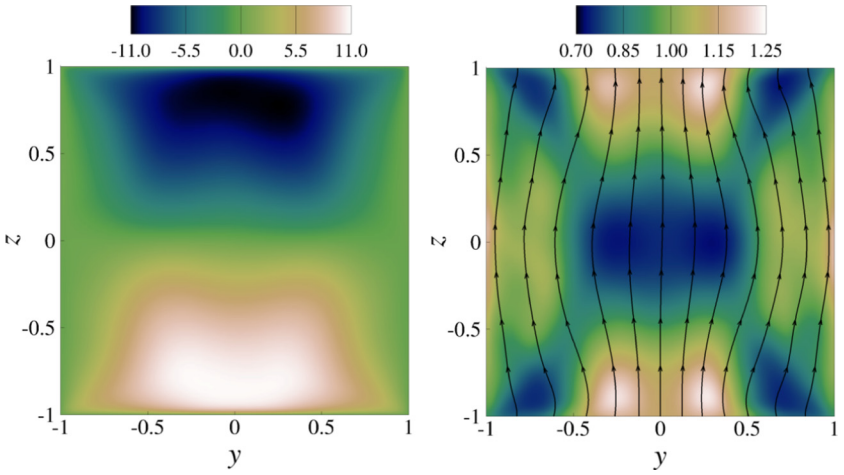

FIG. 5. Structure of the mean magnetic field at Rm = 400 and Ha = 43.5. Left: Contours of the mean axial magnetic field $\langle b_x\rangle_{x,t}$ in the duct cross section. Right: Projected field lines of the mean magnetic field in the cross section, colored by its magnitude $\langle b_\perp\rangle_{x,t}$.

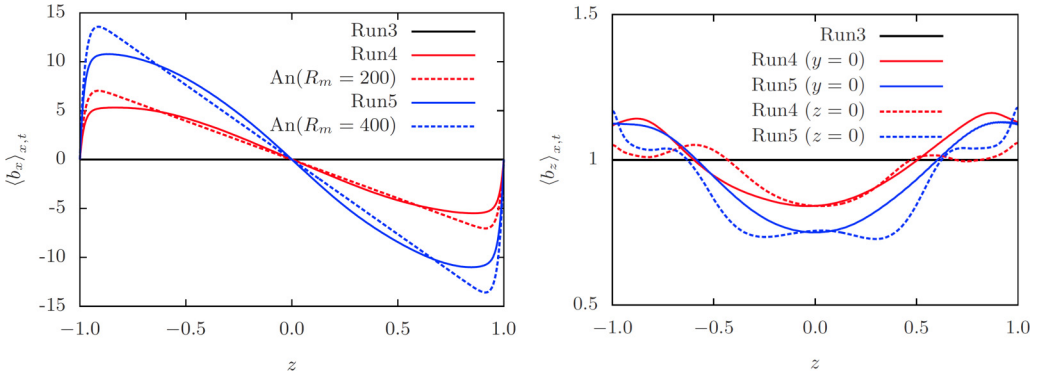

FIG. 6. Profiles of the mean magnetic field components. Left: Mean axial magnetic field $\langle b_x \rangle_{x,t}$ along $y = 0$. The dashed lines indicate the analytical solution for the corresponding laminar flow [23,24]. Right: Mean wall-normal magnetic field $\langle b_z \rangle_{x,t}$ profiles vs z along lines $y = 0$ (solid lines) and versus y along $z = 0$ (dashed lines), respectively. The Hartmann number is Ha = 43.5 and run 3 is the quasistatic run.

of sign which occurs across the plane at $z = 0$. We note that there is no net axial magnetic field in the cross section and $\langle b_x \rangle_{x,t} = 0$ at the walls. The structure of the mean axial magnetic field is similar to that obtained with a laminar flow (an analytical series solution exists for the MHD duct flow at finite Rm with insulating walls [23,24]). It is also important to recall that such high magnitudes of b_x are not converted into a significant magnetic energy (as compared to the kinetic energy), as discussed earlier. In Fig. 5 (right), the field lines of the cross-stream magnetic field, i.e., $\boldsymbol{b}_\perp = (b_y, b_z)$, are shown. They are projected onto the y-z plane and shown together with the distribution of their magnitude, which is given by

$$\langle b_\perp(y,z) \rangle_{x,t} = \sqrt{\langle b_y \rangle_{x,t}^2 + \langle b_z \rangle_{x,t}^2} \tag{24}$$

for the magnetic Reynolds number Rm = 400.

A significant amount of cross-stream magnetic flux is expelled from the center of the duct and the duct corners, which is indicated by deep-blue filled contours. In line with this expulsion, the cross-stream magnetic flux is seen to be enhanced in the side regions and near the Hartmann walls close to $y = 0$. This leads to a deflection of the magnetic field lines toward the side walls. Such a redistribution of magnetic flux in turn has a significant effect on the mean flow distribution. The profiles of the mean axial magnetic field $\langle b_x \rangle_{x,t}$ are shown in Fig. 6. A steep variation over the Hartmann layer is observable in Fig. 6 (left) with little variation in the spanwise direction. Also plotted in Fig. 6 (left) are the analytical series solutions for b_x, when the flow is considered to be laminar at these parameters. It is observed that the qualitative behavior of these profiles is similar to that of the laminar case. Turbulence, however, is seen to reduce the peak value of the magnetic field significantly. Moreover, the peak value of $\langle b_x \rangle_{x,t}$ is found to scale as $\langle b_x \rangle_{x,t}^{\max} \sim \mathrm{Rm}\,\mathrm{Ha}^{-1}$.

At this point, it is instructive to note that the tangential component of the magnetic field has a significant amplitude at the duct walls. This is in contrast to the often used assumption of pseudo-vacuum boundary conditions ($\boldsymbol{b}_t = 0$) for the magnetic field at the walls, as in several dynamo simulations [25,26].

C. Mean velocity field

Figure 7 shows the contours of the distribution of mean axial velocity $\langle u_x \rangle_{x,t}$ in the duct cross section. At Rm = 400, the thin Hartmann and Shercliff boundary layers, similar to those for case Rm = 0, are retained. However, there are some significant changes in their structure when the magnetic Reynolds number is increased. These changes can be clearly seen in Fig. 7(c), where the difference $\langle u_x \rangle_{x,t}(\mathrm{Rm} = 400) - \langle u_x \rangle_{x,t}(\mathrm{Rm} = 0)$ is plotted. One can observe that, in the Hartmann

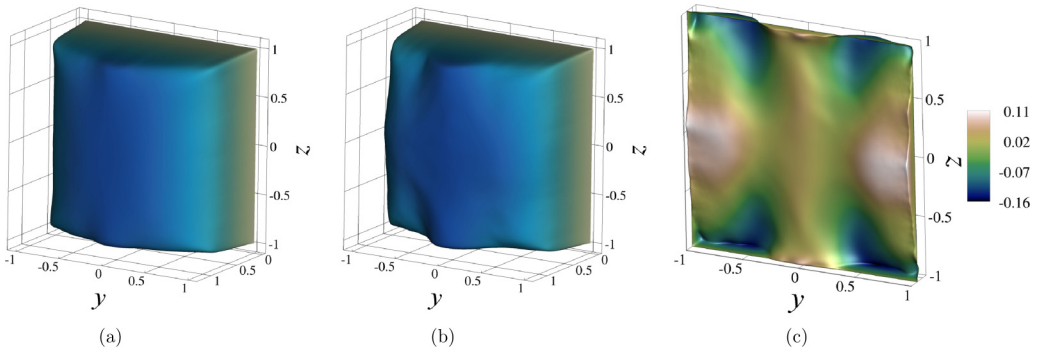

FIG. 7. Contours of the mean axial velocity $\langle u_x \rangle_{x,t}$ in the cross section at Ha = 43.5. (a) Rm = 0. (b) Rm = 400. (c) Difference $\langle u_x \rangle_{x,t}(\mathrm{Rm} = 400) - \langle u_x \rangle_{x,t}(\mathrm{Rm} = 0)$. The contour range spans from $\langle u_x \rangle_{x,t} = 0$ at the light end to $\langle u_x \rangle_{x,t} = 1.35$ at the dark end in panels (a) and (b).

layers, the mean velocity is increased in the central region around $y = 0$ when $\mathrm{Rm} \neq 0$ but decreases everywhere else. This behavior is in line with the cross-stream magnetic field distribution in the Hartmann layers, as the component b_z results in an axial Lorentz force that acts to accelerate the flow in this region.

A higher velocity in the central region of the duct can be attributed to the expelled magnetic flux in that region and hence a lower decelerating force. Furthermore, a higher velocity in the Shercliff layers as well as in regions further toward the duct center can be explained by the mean flow redistribution, that occurs in order to maintain a constant flow rate in the presence of the net flow reduction near the Hartmann walls. Mean velocity profiles are also shown in Fig. 8. They clearly indicate an enhanced mean velocity at the side wall regions where the Shercliff layers are formed and the simultaneous decrease occurring at the walls where the Hartmann layers are present. However, given that $R_m \sim 10^2$ is significantly larger compared to the quasistatic case, the quantitative effect on the mean axial flow velocity is surprisingly small. To summarize, our analysis reveals systematic modifications of the mean axial velocity distribution when Rm increases, with varied trends observed for different regions of the duct cross section.

Figure 9 shows a comparison of the vectors of the transverse components of the mean flow in the cross section for the Rm = 0 and Rm = 400 cases. As in the quasistatic case, the four pairs of counter-rotating rolls (without diagonal symmetry) are still retained in the Rm = 400 case, but

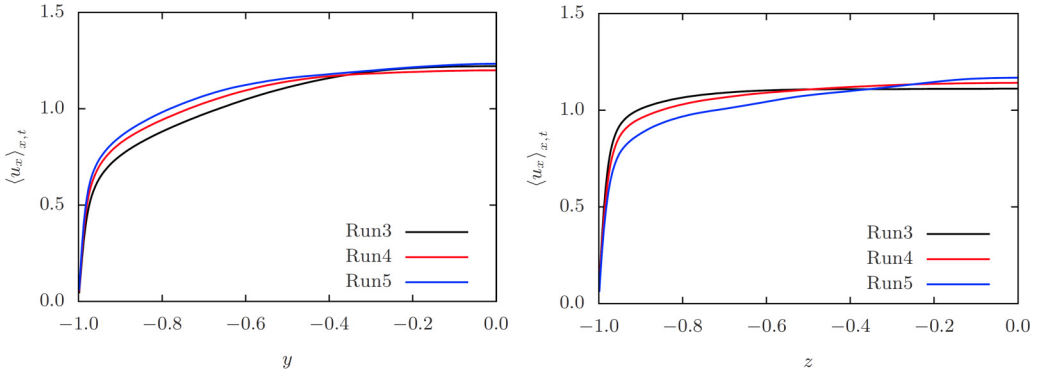

FIG. 8. Comparison of the profiles of the mean axial velocity $\langle u_x \rangle_{x,t}$ along the lines $z = 0$ (left panel) and $y = 0.5$ (right panel). The Hartmann number is again Ha = 43.5 and run 3 is the quasistatic case. Only one half of the cross section is plotted in both panels.

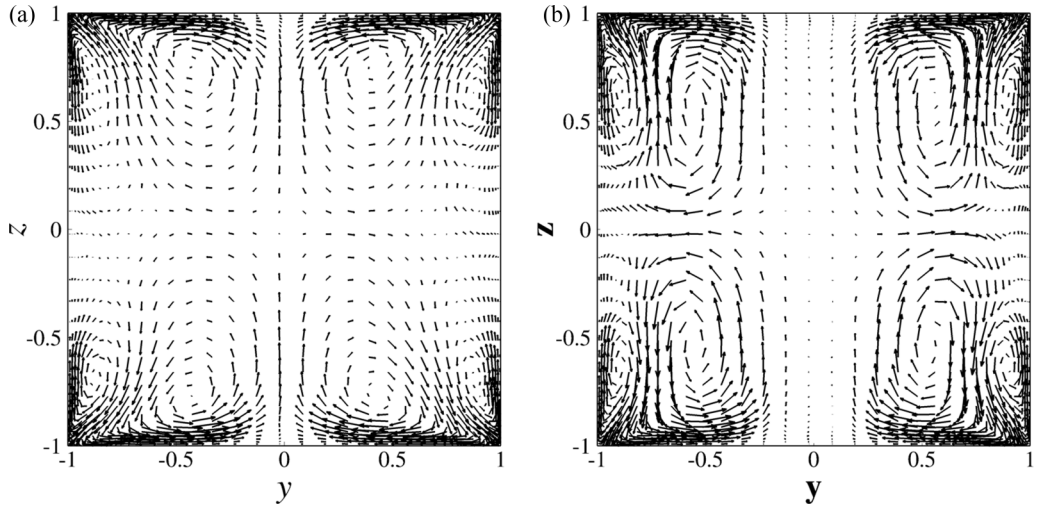

FIG. 9. Vectors of the mean secondary flow in the cross section at Ha = 43.5. (a) Rm = 0. (b) Rm = 400. The maximum magnitude of the cross-stream velocity max $(\sqrt{\langle u_y\rangle_{x,t}^2 + \langle u_z\rangle_{x,t}^2}) \approx 0.019$ for both the cases.

with significant differences. The rolls at moderate Rm have a vertically elongated structure with the horizontal span limited to about $|y| \geqslant 0.25$, whereas in the Rm = 0 case they span the entire width of the duct cross section. Furthermore, although the maximum magnitude of the mean transverse velocity is approximately the same in both cases (and occurs close to the Hartmann walls), the velocity distribution is more homogenized in the Rm = 400 case with much larger velocities observed both at the interface of the rolls and extending until $z = 0$. The reason for such a structural change seems to stem from the dynamics in the Hartmann layer. At first it must be recognized that the bottleneck for the secondary flow in the larger vortex is close to the Hartmann walls as can be seen from the high density (as well as longer) horizontal vectors in this region. This horizontal flow close to the Hartmann walls is inhibited effectively in the moderate Rm case by the enhanced horizontal Lorentz force (in the y direction) that extends to about $y \approx 0.25$. The latter is caused predominantly by the $\langle j_z\rangle_{x,t}\langle b_x\rangle_{x,t}$ component of the Lorentz force that points in the direction opposing the horizontal flow in the Hartmann layers. Because of this, the flow in the larger vortex is limited to a shorter horizontal span, but as a result also has a stronger vertical velocity outside Hartmann layers.

D. Skin friction coefficients

In view of applications, the skin friction coefficient is one of the central quantities when characterizing turbulent wall-bounded flows. In the following, we present this analysis for the magnetohydrodynamic duct flow at hand. As we have already seen in the previous paragraphs, differences can be observed between the quasistatic and full magnetohydrodynamic case. Furthermore, it is expected that the behavior at the Hartmann and Shercliff layers will be different. The skin friction coefficients of both types of layers are defined as follows:

$$C_{f,\mathrm{HL}} = \frac{1}{\mathrm{Re}}\left\langle \left.\frac{\partial u_x}{\partial n}\right|_{z=-1} + \left.\frac{\partial u_x}{\partial n}\right|_{z=+1} \right\rangle_{x,y,t}, \tag{25}$$

$$C_{f,\mathrm{SL}} = \frac{1}{\mathrm{Re}}\left\langle \left.\frac{\partial u_x}{\partial n}\right|_{y=-1} + \left.\frac{\partial u_x}{\partial n}\right|_{y=+1} \right\rangle_{x,z,t}. \tag{26}$$

TABLE II. Comparison of the skin-friction coefficients at Re = 14 500. The numbering of the DNS runs corresponds with that in Table I.

	$C_{f,\mathrm{HL}}$	$C_{f,\mathrm{SL}}$	C_f
Run 0	5.64×10^{-3}	5.64×10^{-3}	5.64×10^{-3}
Run 1	6.40×10^{-3}	3.66×10^{-3}	5.03×10^{-3}
Run 2	6.24×10^{-3}	4.08×10^{-3}	5.16×10^{-3}
Run 3	5.90×10^{-3}	4.08×10^{-3}	4.99×10^{-3}
Run 4	6.04×10^{-3}	4.69×10^{-3}	5.37×10^{-3}
Run 5	5.31×10^{-3}	5.13×10^{-3}	5.22×10^{-3}

The modified mean velocity field (which we discussed in the last subsection) has a substantial effect on the skin friction coefficients. These trends are summarized in Table II, where we list the skin friction coefficients with respect to either pair of walls as well as the overall skin friction coefficient. The latter quantity is defined as the arithmetic mean,

$$C_f = \tfrac{1}{2}(C_{f,\mathrm{HL}} + C_{f,\mathrm{SL}}). \tag{27}$$

As expected, $C_{f,\mathrm{HL}}$ at Rm = 400 decreases whereas $C_{f,\mathrm{SL}}$ increases as compared to the quasistatic case. However, the net effect on the overall skin friction coefficient C_f seems to be almost negligible due to the opposing trends in both types of boundary layers. The same behavior is observed in the case of the smaller Hartmann number, Ha = 29, when the flow is fully turbulent, although the impact at both the boundary layers differs.

It is interesting to see how the skin friction coefficient varies with the Hartmann number, when Rm is finite but moderate. The behavior in the quasistatic case is well known from the existing experiments and numerical studies: On the one hand, skin friction at the Shercliff walls decreases with an increase of the Hartmann number due to the suppression of turbulence in the side layers. On the other hand, the skin friction at the Hartmann walls increases with Hartmann number due to the so-called Hartmann flattening effect of the mean profile. However, in the case of Rm = 400, we find that skin friction coefficient variation remains small when Ha is enhanced moderately. The change becomes larger when Ha is further increased. This is shown in Fig. 10, where the variation of $C_{f,\mathrm{HL}}$ and $C_{f,\mathrm{SL}}$ with the Hartmann number is plotted. In fact, for the Hartmann walls, it is observed that

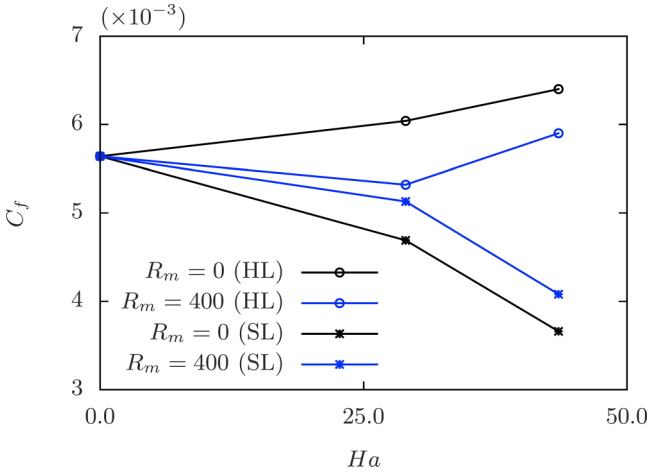

FIG. 10. Variation of the individual skin-friction coefficients $C_{f,\mathrm{HL}}$ and $C_{f,\mathrm{SL}}$ with the Hartmann number at Rm = 0 and Rm = 400.

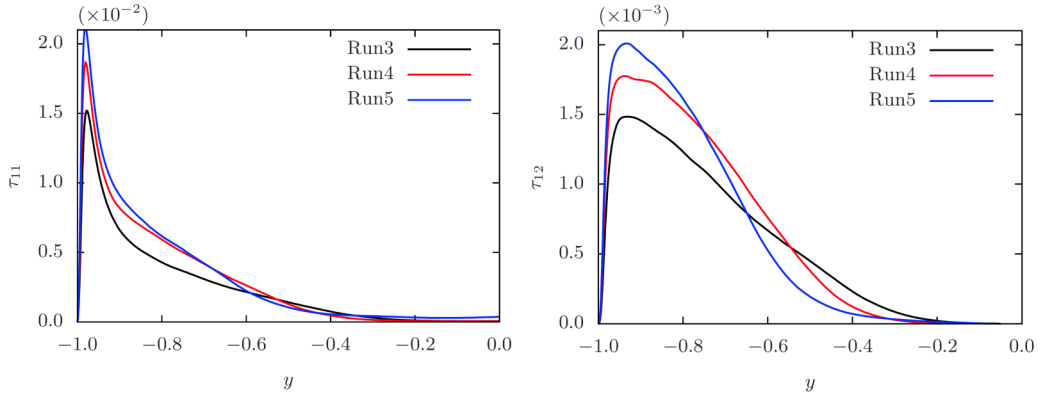

FIG. 11. Comparison of the total turbulent stress components $\tau_{11} = -\langle u'_x u'_x + N\mathrm{Rm}^{-1} b'_x b'_x \rangle_{x,t}$ (left panel) and $\tau_{12} = -\langle u'_x u'_y + N\mathrm{Rm}^{-1} b'_x b'_y \rangle_{x,t}$ (right panel) along the line $z = 0$.

the skin friction coefficient decreases for $\mathrm{Ha} = 29$ and then increases again for $\mathrm{Ha} = 43.5$. Such data can be potentially useful when predicting the skin friction coefficients in the case of $\mathrm{Rm} \sim 1$ (that are encountered in practical applications), by interpolation.

IV. SMALL-SCALE STRUCTURE

A. Turbulent stresses

We now turn to the effect of a moderate Rm on the turbulent stresses. We apply the standard Reynolds decomposition of all fields

$$\boldsymbol{u}'(x, y, z, t) = \boldsymbol{u}(x, y, z, t) - \langle \boldsymbol{u}(y, z) \rangle_{x,t}, \tag{28}$$

$$\boldsymbol{b}'(x, y, z, t) = \boldsymbol{b}(x, y, z, t) - \langle \boldsymbol{b}(y, z) \rangle_{x,t}, \tag{29}$$

$$p'(x, y, z, t) = p(x, y, z, t) - \langle p(y, z) \rangle_{x,t}, \tag{30}$$

where the subscript prime indicates the fluctuation. Averaging the momentum equation (5) in the homogeneous directions x and t yields the Reynolds-averaged Navier-Stokes equation as

$$\partial_t \boldsymbol{U} + \boldsymbol{\nabla} \cdot (\boldsymbol{U}\boldsymbol{U}) = G\boldsymbol{e}_x - \boldsymbol{\nabla}\left\langle p + \frac{N}{\mathrm{Rm}} \boldsymbol{b}^2 \right\rangle_{x,t} + \mathrm{Re}^{-1} \nabla^2 \boldsymbol{U} + \boldsymbol{\nabla} \cdot \boldsymbol{\tau} + \frac{N}{\mathrm{Rm}} \boldsymbol{\nabla} \cdot (\boldsymbol{B}\boldsymbol{B}), \tag{31}$$

where the mean velocity and magnetic fields are denoted as $\boldsymbol{U} = \langle \boldsymbol{u} \rangle_{x,t}$ and $\boldsymbol{B} = \langle \boldsymbol{b} \rangle_{x,t}$ respectively. The total turbulent stress tensor is given by

$$\tau_{ij} = \left\langle -u'_i u'_j + \frac{N}{\mathrm{Rm}} b'_i b'_j \right\rangle_{x,t}. \tag{32}$$

The two terms in the above equation correspond to the hydrodynamic part (Reynolds stress) and the magnetic stress respectively. It must be noted that Eq. (31) is not valid in the quasistatic case and in turn τ_{ij} will just contain the Reynolds stress part. We are primarily interested in those components of the tensor that affect the mean axial velocity, that is, τ_{1j}. Furthermore, since $N/\mathrm{Rm} \sim 10^{-3}$, the contribution of the magnetic stresses to the total turbulent stress can be considered negligible.

Figure 11 shows the distribution of the dominant turbulent stress components τ_{11} and τ_{12} along the spanwise direction ($z = 0$), for the cases with $\mathrm{Ha} = 43.5$. With increase in Rm, both the stress components show a significant increase in the Shercliff layer and beyond up to about $|y| \approx 0.7$. This is possibly due to the enhancement of streamwise fluctuations by the large value of induced

b_x. Closer to the duct center, τ_{11} shows negligible variation with Rm, whereas τ_{12} becomes slightly lower as Rm increases.

B. Turbulent energies and electromotive forces in magnetohydrodynamic case

In the following, we investigate the energy balance of the small-scale fluctuations more closely. In the MHD case, we have contributions due to velocity and secondary magnetic field, respectively. We define the total turbulent energy k for a finite-Rm duct flow as

$$k = k_u + k_b = \frac{1}{2}\langle \boldsymbol{u}'^2 \rangle_{x,t} + \frac{N}{2\mathrm{Rm}}\langle \boldsymbol{b}'^2 \rangle_{x,t}. \tag{33}$$

Definition (33) contains contributions from both the kinetic energy as well as the magnetic energy of fluctuations. These definitions differ from the volume averages $E_{\mathrm{kin}}(t)$ and $E_b(t)$ which we have defined in (20) and (22), respectively. In the present MHD cases, the kinetic energy part will dominate, as we discussed earlier. The transport equation for the evolution of $k(\boldsymbol{x}, t)$ is given by

$$\frac{Dk}{Dt} = \frac{\partial k}{\partial t} + (\boldsymbol{u}\cdot\boldsymbol{\nabla})k = P_k - \epsilon_k + \boldsymbol{\nabla}\cdot\boldsymbol{T}_k, \tag{34}$$

where the production P_k, dissipation ϵ_k, and the transfer term $\boldsymbol{T}_k$ are defined as

$$P_k = -\langle u_i' u_j' \rangle_{x,t} \frac{\partial \langle u_j \rangle_{x,t}}{\partial x_i} - \frac{N}{\mathrm{Rm}} \langle b_i' b_j' \rangle_{x,t} \frac{\partial \langle b_j \rangle_{x,t}}{\partial x_i}, \tag{35}$$

$$\epsilon_k = \left\langle \frac{1}{\mathrm{Re}} \left(\frac{\partial u_i'}{\partial x_j} \right)^2 + \frac{N}{\mathrm{Rm}^2} \left(\frac{\partial b_i'}{\partial x_j} \right)^2 \right\rangle_{x,t}, \tag{36}$$

$$\boldsymbol{T}_k = \frac{N}{\mathrm{Rm}} h\boldsymbol{b} - \left\langle \left[\frac{1}{2} u_i'^2 + \frac{N}{2\mathrm{Rm}} b_i'^2 + p' \right] \boldsymbol{u}' \right\rangle_{x,t} + \frac{N}{\mathrm{Rm}} \langle (u_i' b_i') \boldsymbol{b}' \rangle_{x,t} + \frac{1}{\mathrm{Re}} \boldsymbol{\nabla} k_u + \frac{1}{\mathrm{Rm}} \boldsymbol{\nabla} k_b, \tag{37}$$

with $h(\boldsymbol{x}, t)$ being the turbulent cross-helicity which is defined as

$$h(\boldsymbol{x}, t) = \langle u_i' b_i' \rangle_{x,t}, \tag{38}$$

in the first term on the right-hand side of (37). In all expressions, we used index notation and Einstein sum convention. For a comparison with the quasistatic MHD flow at $\mathrm{Rm} = 0$, it is useful to list the corresponding energy balance, which is given by

$$\frac{Dk_u}{Dt} = P_k^{(q)} - \epsilon_k^{(q)} + \boldsymbol{\nabla}\cdot\boldsymbol{T}_k^{(q)}. \tag{39}$$

The three terms of the balance of the turbulent kinetic energy density now take the following form:

$$P_k^{(q)} = -\langle u_i' u_j' \rangle_{x,t} \frac{\partial \langle u_j \rangle_{x,t}}{\partial x_i}, \tag{40}$$

$$\epsilon_k^{(q)} = \left\langle \frac{1}{\mathrm{Re}} \left(\frac{\partial u_i'}{\partial x_j} \right)^2 \right\rangle_{x,t} + N[\langle \boldsymbol{j}^2 \rangle_{x,t} + \langle \boldsymbol{u} \rangle_{x,t} \cdot \langle \boldsymbol{j} \times \boldsymbol{B_0} \rangle_{x,t}], \tag{41}$$

$$\boldsymbol{T}_k^{(q)} = -\left\langle \left[\frac{1}{2} u_i'^2 + p' \right] \boldsymbol{u}' \right\rangle_{x,t} + \frac{1}{\mathrm{Re}} \boldsymbol{\nabla} k_u - N \langle \phi \boldsymbol{j} \rangle_{x,t}. \tag{42}$$

A comparison of the distribution of the turbulent kinetic energy $\langle k_u \rangle_{x,t}$ in the cross section for $\mathrm{Rm} = 0$ and $\mathrm{Rm} = 400$ is shown in Fig. 12. It can be seen that the case of $\mathrm{Rm} = 400$ shows a significant spatial redistribution of the turbulent kinetic energy as compared to the quasistatic case. The kinetic energy increases over most part of the cross section and the increase is particularly pronounced in the side wall regions (SL). It should be noted here that, in flows with mean shear, the main contribution

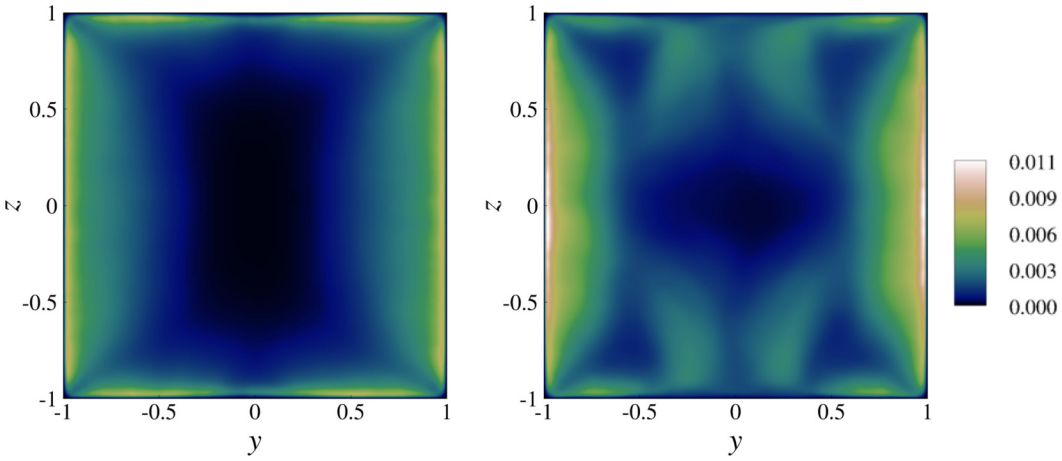

FIG. 12. Contours of the turbulent kinetic energy $k_u(y, z)$ in the duct cross section at Ha = 43.5. Left: Rm = 0. Right: Rm = 400. The contour levels for both panels are given by the color bar.

to the turbulent kinetic energy production always arises from the streamwise velocity fluctuations, i.e., from the component u'_x. For example, for the flow at hand at Rm = 400, streamwise fluctuations $\langle u_x'^2 \rangle_{x,t}$ contribute with about 80% to the production of k.

We conclude that turbulent energy is redistributed and enhanced in the streamwise fluctuations with negligible effect on the turbulent energy contributions arising from the transverse components at a moderate Rm. The higher levels of turbulent kinetic energy can be attributed to the higher rate of production of k. This is shown in Fig. 13, where the first term on the right-hand side of Eq. (35) is compared to that of (40) for the quasistatic MHD flow. Profiles are shown along the horizontal line $z = 0$. An increase of Rm is in line with a gradual rise of the production rate of the turbulent energy density k.

We now take a closer look at the turbulent magnetic component. The corresponding evolution equation is given by [27]

$$\frac{\partial \boldsymbol{b}'}{\partial t} = \boldsymbol{\nabla} \times (\boldsymbol{u}' \times \langle \boldsymbol{b} \rangle_{x,t} + \langle \boldsymbol{u} \rangle_{x,t} \times \boldsymbol{b}') + \frac{1}{\mathrm{Rm}} \boldsymbol{\nabla}^2 \boldsymbol{b}' + \boldsymbol{\nabla} \times (\boldsymbol{u}' \times \boldsymbol{b}' - \langle \boldsymbol{u}' \times \boldsymbol{b}' \rangle_{x,t}). \tag{43}$$

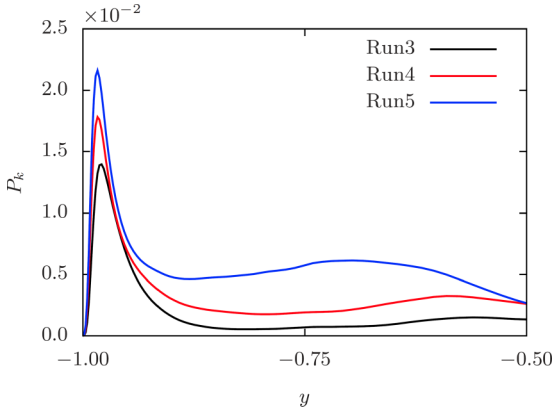

FIG. 13. Variation of turbulent kinetic energy production P_k in the spanwise direction y along $z = 0$. Run 3 is the quasistatic case.

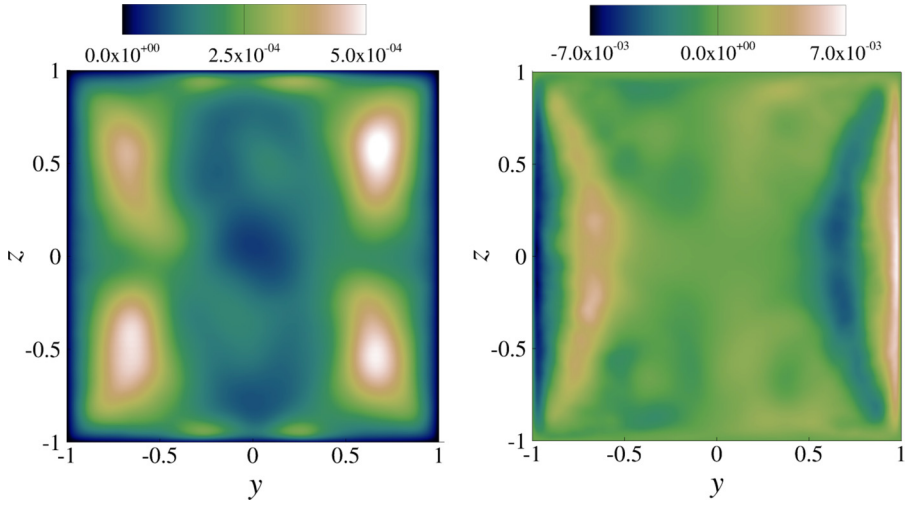

FIG. 14. Contour of the turbulent magnetic energy $k_b(y, z)$ (left) and x component of turbulent electromotive force $\mathcal{E}_x(y, z) = \langle u'_y b'_z - u'_z b'_y \rangle_{x,t}$ (right) in the y-z cross section for Rm = 400 and Ha = 43.5 (run 5).

In the left panel of Fig. 14, we plot contours of the turbulent magnetic energy $k_b(y, z)$. The evolution of $k_b(y, z)$ is obtained by multiplication of (43) with $\boldsymbol{b}'$. We observe the strongest contributions in the corner regions of the duct cross section, exactly where the field lines are bent most strongly due to flux expulsion as shown in Fig. 5 (right).

The last term of Eq. (43) stands for the curl of the turbulent electromotive force $\mathcal{E} = \langle \boldsymbol{u}' \times \boldsymbol{b}' \rangle_{x,t}$. In the right panel of Fig. 14, we plot the x component of the electromotive force $\mathcal{E}_x$. For the magnetic Reynolds numbers at hand and with a streamwise magnetic field component present, the ingredients exist which could generate a dynamo, which is however not observed here. The largest amplitudes of $\mathcal{E}_x$ are observed again in the Shercliff layers. However, the overall magnitude remains very small.

C. Local isotropy measures

We will now turn to the analysis of the effect of the moderate Rm on the local isotropy. Different mechanisms which generate deviations from the local isotropy of small-scale statistical properties are at work in the present duct flow. On the one hand, it is well known from the existing low-Rm DNS studies of flows in periodic boxes [15] that the application of a uniform magnetic field leads to a more rapid decay of the gradients along the magnetic field lines and hence to an increase of the local anisotropy in the direction parallel to the external magnetic field. On the other hand, wall-bounded shear flows enhance streamwise fluctuations due to the turbulence production mechanism. This leads to the well-known formation of streaky structures in the streamwise direction and hence can be considered as a further anisotropy generation in that direction.

The physical mechanisms leading to both of these effects are different. Their relative dominance depends on the ratio of two timescales,

$$\frac{t_J}{t_{\mathrm{adv}}} = \frac{1}{N} \quad \text{with} \quad t_J = \frac{\rho}{\sigma B_0^2}. \tag{44}$$

Timescale t_J is the Joule damping timescale, t_{adv} the advection time scale [see Eq. (1)]. Typically, this ratio is much larger than unity in MHD turbulence in ducts or channels, as only a small value of N can sustain turbulence without a relaminarization of the flow. Hence, the effect of shear is expected to be more pronounced. This fact has also been confirmed by Krasnov *et al.* [28] in the study of MHD channel flow with a spanwise magnetic field. In our present study, $t_J/t_{\mathrm{adv}} \approx 7.7$, thus indicating a weaker anisotropy contribution that is induced by the magnetic field.

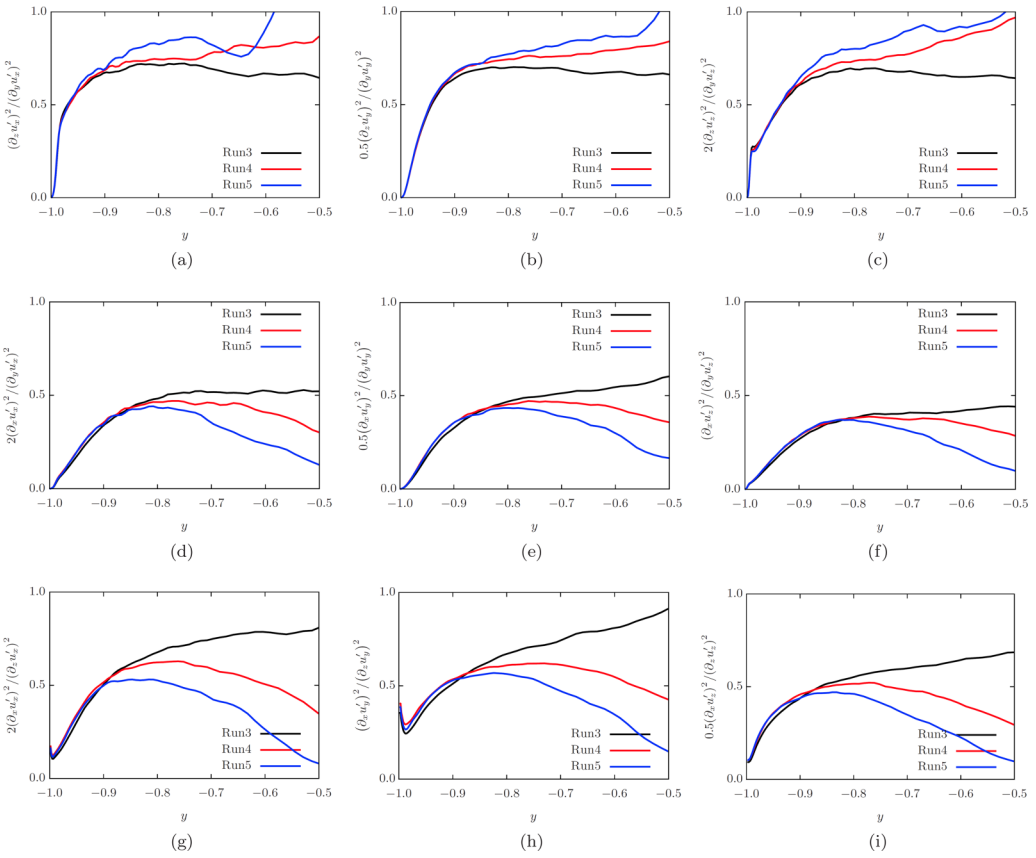

FIG. 15. Effect of a moderate Rm on flow anisotropy. Time-averaged anisotropy coefficients obtained from Eq. (45) are shown along the line $z = 0.5$ for the case of Ha $= 43.5$.

There are several possible measures of anisotropy. One of the suitable measures is the ratio of mean squares of velocity gradients, defined as

$$A_{ij} = \frac{\left\langle \left(\frac{\partial u_i'}{\partial z} \right)^2 \right\rangle (1 + \delta_{i3})}{\left\langle \left(\frac{\partial u_i'}{\partial x_j'} \right)^2 \right\rangle (1 + \delta_{ij})}, \tag{45}$$

with the z direction being the direction of the external magnetic field $\boldsymbol{B}_0$ and the angular brackets refer to streamwise and time averaging. The multiplication factors ensure that these ratios remain within unity. These ratios compare the relative levels of anisotropy between the directions j and z for the velocity component u_i. A smaller ratio will imply that gradients in the direction used for the derivative in the numerator are smaller and hence a relative anisotropy in that direction. Furthermore, the behavior of these ratios might be different for the different components of velocity fluctuations, and all components of the velocity gradient tensor should be therefore considered.

Figures 15(a) to 15(c) (top row) shows the distribution of these ratios along the horizontal line $z = 0.5$, for the spanwise and wall-normal directions for the case of Ha $= 43.5$. At Rm $= 400$, one can see that no differences appear close to the Shercliff wall. However, away from the wall, the anisotropy along the imposed magnetic field direction (z direction) clearly decreases. The situation is the same considering each of the fluctuation components. The reason for this reduced level of

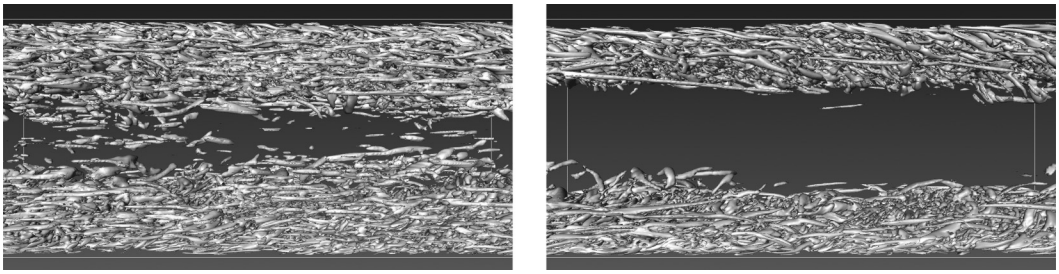

FIG. 16. Isosurfaces of near-wall vortical structures which are obtained by the λ criterion with $\lambda_2 = -0.75$ for Rm = 0 (left) and Rm = 400 (right) with the common parameters Ha = 43.5 and Re = 14500. View is along the y direction (flow is from left to right).

anisotropy in the z direction is the existence of a significant mean component $\langle b_y \rangle_{x,t} \sim \mathcal{O}(1)$ in the case with Rm = 400, which is absent in the quasistatic run 3. In addition, the difference increases as we move away from the wall which is in line with the increasing $\langle b_y \rangle_{x,t}$ in that direction. It should be noted that these ratios are plotted only in the region where the flow is fully turbulent for Ha = 43.5, i.e., $y \in [-1, -0.5]$, since these ratios are no more relevant in the core region of the duct. As discussed in Sec. III, velocity fluctuations are suppressed strongly and hence their gradients are small as well.

Comparison for the streamwise and spanwise directions is shown through Figs. 15(d) to 15(f) (middle row). Here, gradients in the streamwise direction are reduced significantly due to the large amplitude of the generated $\langle b_x \rangle_{x,t}$, except in the region close to the walls where $\langle b_x \rangle_{x,t}$ has a low amplitude. Finally, the comparison of the x and z directions in the bottom row of the figure shows a significant enhancement of streamwise anisotropy away from the side walls. This behavior remains qualitatively the same throughout the turbulent portion of the flow in the cross section. This behavior was also confirmed from an analysis of the contours of the difference of the ratios for Rm = 400 and Rm = 0, which is not shown here. Mostly negative values exist to a large extent except in the region close to the centerline $z = 0$, indicating the increase in effect of the streamwise field. This is also in line with the results of Kassinos *et al.* [29], where homogeneous MHD turbulence subjected to mean shear in fixed and rotating frames was studied. At the centerline ($z = 0$), the effect is negligible as this is a symmetry line where $\langle b_x \rangle_{x,t} = 0$ as seen earlier.

This enhancement of shear-induced anisotropy at Rm = 400 should result in correspondingly longer streamwise vortical structures. This is indeed the case, as is evident from the comparison of isosurfaces of $\lambda_2 = -0.75$ shown in Fig. 16. These surfaces are considered to indicate coherent vortical structures [30]. The structures are more elongated in the x direction for the case of Rm = 400. Here, λ_2 is the second largest eigenvalue of the tensor Λ_{ik}, which is given by

$$\Lambda_{ik} = S_{ij} S_{jk} + \Omega_{ij} \Omega_{jk}, \tag{46}$$

with the rate of strain tensor S_{ij} and the vorticity tensor Ω_{ij}. They are defined as

$$S_{ij} = \frac{1}{2}\left(\frac{\partial u_i}{\partial x_j} + \frac{\partial u_j}{\partial x_i}\right), \qquad \Omega_{ij} = \frac{1}{2}\left(\frac{\partial u_i}{\partial x_j} - \frac{\partial u_j}{\partial x_i}\right). \tag{47}$$

An alternative measure of the anisotropy due to mean shear in wall-bounded flows is the skewness of the wall-normal derivative of the streamwise velocity fluctuation. This is a measure of the streamwise anisotropy without any relative comparison to other directions. Here the skewness is defined as

$$M_3 = \frac{\left\langle \left(\frac{\partial u_x'}{\partial z}\right)^3 \right\rangle}{\left\langle \left(\frac{\partial u_x'}{\partial z}\right)^2 \right\rangle^{3/2}}. \tag{48}$$

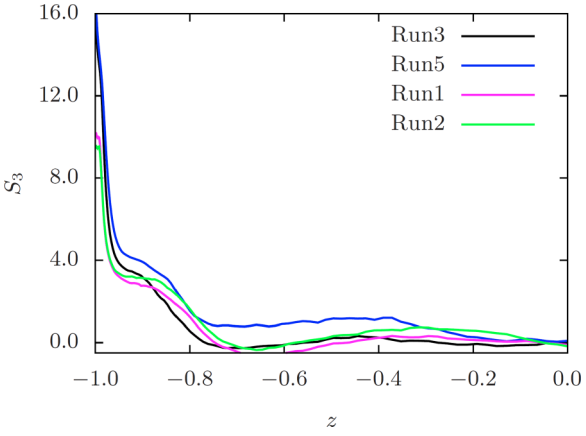

FIG. 17. Profiles of the skewness of the wall normal derivative $\partial u_x'/\partial z$ along the line $y = -0.75$.

In a perfectly locally isotropic turbulence, the third-order moment (as well as all other odd-order moments) must vanish. Hence, a finite value indicates a deviation from a locally isotropic state. The skewness measure has often been used as an indicator of local anisotropy in shear flow turbulence (see, e.g., Refs. [31,32]). Figure 17 shows the distribution of the skewness of the derivative $\partial_z u_x'$ along the vertical line $y = -0.75$, in the turbulent zone for the runs at $\mathrm{Ha} = 43.5$. Positive values of skewness indicate a higher probability for the velocity fluctuation component $\partial_z u_x'$ to increase as we move away from the wall boundary. The curves show a steep decay from large values near the wall and flatten thereafter. At the centerline, skewness must vanish due to symmetry reasons. Outside the Hartmann boundary layer, significantly larger values of skewness (at least about 40%) are observed at $\mathrm{Rm} = 400$ as compared to $\mathrm{Rm} = 0$. In addition, at moderate magnetic Reynolds number, the profile shows finite values up to $z \approx -0.4$, whereas in the quasistatic case the skewness vanishes very quickly. This indicates that the effect of mean shear extends deeper into the bulk flow when $\mathrm{Rm} = 400$. That this conclusion is valid across the duct cross section is verified from the mostly positive values of the skewness difference at $\mathrm{Rm} = 400$ and $\mathrm{Rm} = 0$, which is shown in Fig. 18.

V. SUMMARY AND OUTLOOK

We have investigated the impact of a finite secondary magnetic field in a turbulent magnetohydrodynamic duct flow by means of three-dimensional direct numerical simulations, using boundary

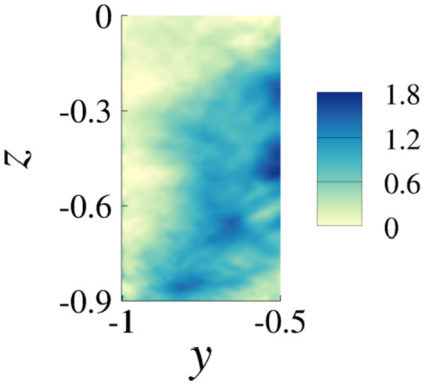

FIG. 18. Contours of the difference between $\mathrm{Rm} = 400$ and $\mathrm{Rm} = 0$ in the skewness of wall normal derivative $\partial u_x'/\partial z$, in the duct cross section for $\mathrm{Ha} = 43.5$.

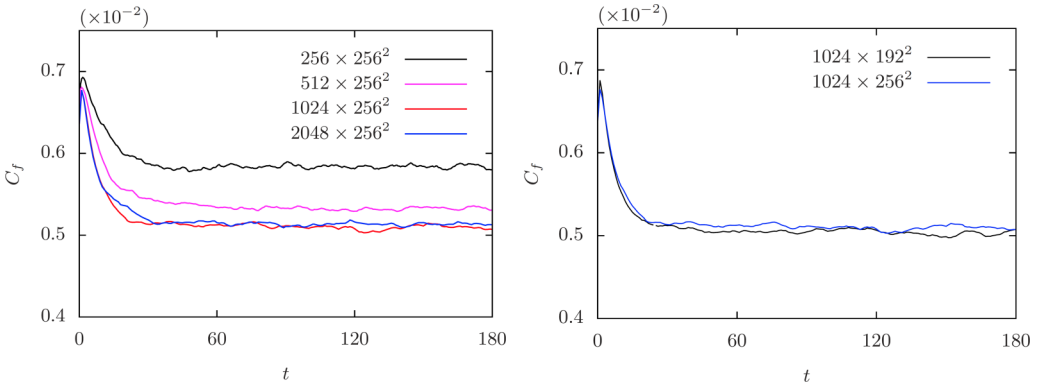

FIG. 19. Sensitivity of the statistically steady skin friction coefficient C_f vs time t. Left: Variation of the grid resolution in the streamwise direction. Right: Variation of grid resolution in the cross section of the duct. The domain size is $4\pi \times 2 \times 2$. Parameters are $\mathrm{Rm} = 0$, $\mathrm{Re} = 14\,500$, and $\mathrm{Ha} = 43.5$.

integrals to capture the boundary conditions of the magnetic field at the duct walls consistently. The numerical simulations are compared with the quasistatic limit for which the secondary magnetic field is completely neglected and the magnetic Reynolds number is zero. Our series of simulations were conducted at a magnetic Prandtl number Pm that is much smaller than unity but still significantly larger than the realistic values in typical liquid metal flow configurations. This problem which is accessible to fully resolved simulations at $\mathrm{Rm} \sim 10^2$ is considered as a first attempt to better understand the differences from the limiting quasistatic case of $\mathrm{Rm} = 0$ in a one-to-one comparison. This is the central motivation of the present work.

Some important differences have been found to occur in the mean flow characteristics such as the increased Shercliff layer skin friction and reduced Hartmann skin friction due to the effects of magnetic flux expulsion in the bulk region of the duct. However, it is remarkable that to a large extent, the mean flow properties are not strongly affected by the finite magnetic Reynolds number. For example, the magnitude of the difference in the streamwise velocity profiles remains small. On the other hand, significant differences were found in the structure of the secondary mean flow. In a nutshell, budgets and fields are slightly redistributed when compared to the quasistatic turbulent state. This might be counterintuitive at a first glance, but is attributed to the low values of the interaction parameter N in the present setup. Such low values of N were a necessary trade-off because further increase in N will tend to laminarize the flow. Differences are much more significant when small-scale statistics are considered. We found, for example, a strong enhancement in streamwise anisotropy away from the boundary layers. Physical aspects that are present only in the case of finite Rm such as the expulsion of magnetic flux or the generation of turbulent electromotive forces lead to a variation of small-scale fluctuations in the flow.

It is clear that values of $\mathrm{Rm} \sim 10^2$ are neither encountered in most practical applications in metallurgy or materials processing nor obtainable in laboratory experiments of MHD wall-bounded flows in liquid metals. However, predictions for lower Rm values could be made to some extent by interpolation from the current results. In this respect, our studies should be valuable. Our investigations also show that for most practical applications (for which first-order quantities are of interest), the quasistatic approximation remains the recipe to simulate the flow. For a deeper understanding of the magnetohydrodynamic turbulence as well as for finite-time response effects in strongly varying turbulent flows, a full magnetohydrodynamic description might be however necessary.

Given the state-of-the-art computational resources, it will remain a challenge to extend the present DNS toward realistic parameters. As stated in the introduction, most practical finite-Rm flows have $\mathrm{Pm} \lesssim 10^{-5}$ and are in a regime with $\mathrm{Rm} \lesssim 10$ and $\mathrm{Re} \gtrsim 10^6$. Numerical modeling of such

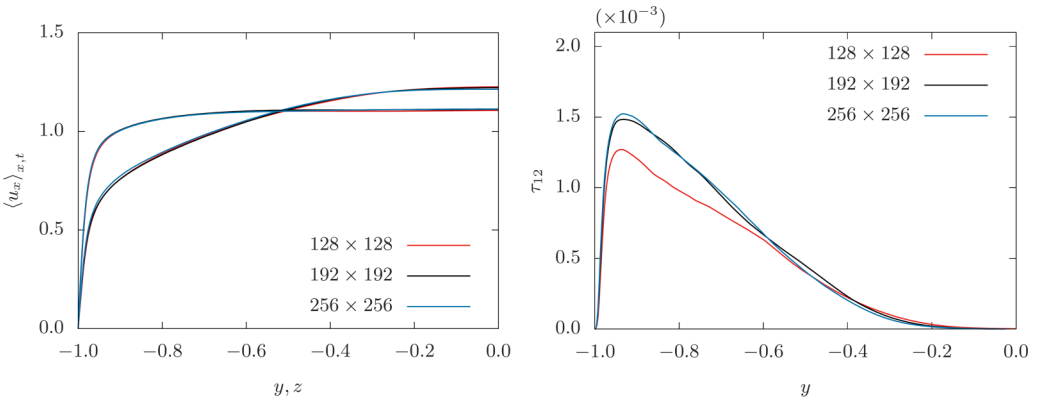

FIG. 20. Sensitivity to the cross-stream grid resolution of the profiles of: Left: mean axial velocity $\langle u_x \rangle_{x,t}$ along y at $z = 0$ and along z at $y = 0.5$. Right: Reynolds stress component τ_{12}. The domain size is $2\pi \times 2 \times 2$ and $N_x = 512$ for all these cases. Parameters are $\mathrm{Rm} = 0$, $\mathrm{Re} = 14\,500$, and $\mathrm{Ha} = 43.5$.

wall-bounded flows will require subgrid-scale models for the turbulent velocity field which are combined with the fully resolved dynamics of the highly diffusive magnetic field. The development of corresponding large eddy simulation models is currently under way and will be a part of our future work. Another possibility is to use a coarser mesh only for the magnetic field evolution that opens the possibility to simulate rotating (planetary) and nonrotating MHD flows in more realistic parameter settings including spherical and cylindrical geometries.

ACKNOWLEDGMENTS

V.B. was supported by the Research Training Group "Lorentz Force Velocimetry and Lorentz Force Eddy Current Testing," which is funded by the Deutsche Forschungsgemeinschaft under Grant No. GRK 1567. Supercomputing resources were provided by the John von Neumann Institute for Computing at the Jülich Supercomputing Centre by Projects No. HIL04 and No. HIL11. We also acknowledge fruitful discussions with Dmitry Krasnov.

APPENDIX: GRID SENSITIVITY

For completeness, we list here results of grid sensitivity studies. In Fig. 19, the relaxation of the skin friction coefficient with respect to time is shown for a number of quasistatic ($\mathrm{Rm} = 0$) simulation runs at different grid resolutions that are indicated in the legend. Figure 20 shows the sensitivity to cross-stream grid resolution of the profiles of mean axial velocity and the Reynolds stress component τ_{12}. This was done with a duct length of 4π, for which $N_x = 1024$ was necessary for convergence. All the simulations reported in this paper were done with a duct length of 2π, for which $N_x = 512$ was used.

[1] P. A. Davidson, *An Introduction to Magnetohydrodynamics* (Cambridge University Press, Cambridge, UK, 2001).
[2] H. K. Moffatt, *Magnetic Field Generation in Electrically Conducting Fluids* (Cambridge University Press, Cambridge, UK, 1983).
[3] W. E. Langlois, Buoyancy-driven flows in crystal-growth melts, Annu. Rev. Fluid Mech. **17**, 191 (1985).
[4] C. Gissinger, P. R. Imazio, and S. Fauve, Instability in electromagnetically driven flows. I, Phys. Fluids **28**, 034101 (2016).

[5] J. Hartmann and F. Lazarus, Hg dynamics II: Experimental investigations on the flow of mercury in a homogeneous magnetic field, K. Dan. Vidensk. Selsk. Mat. Fys. Medd. **15**, 7 (1937).
[6] W. Murgatroyd, Experiments on magnetohydrodynamic channel flow, Philos. Mag. **44**, 1348 (1953).
[7] E. C. Broulliette and P. S. Lykoudis, Magneto-fluid-mechanic channel flow. I. Experiment, Phys. Fluids **10**, 995 (1967).
[8] C. B. Reed and P. S. Lykoudis, The effect of a transverse magnetic field on shear turbulence, J. Fluid Mech. **89**, 147 (1978).
[9] J. A. Shercliff, Steady motion of conducting fluids in pipes under transverse magnetic fields, Math. Proc. Cambridge Philos. Soc. **49**, 136 (1953).
[10] W. E. Williams, Magnetohydrodynamic flow in a rectangular tube at high Hartmann number, J. Fluid Mech. **16**, 262 (1963).
[11] J. C. R. Hunt, Magnetohydrodynamic flow in rectangular ducts, J. Fluid Mech. **21**, 577 (1965).
[12] H. Kobayashi, Large eddy simulation of magnetohydrodynamic turbulent duct flows, Phys. Fluids **20**, 015102 (2008).
[13] V. Shatrov and G. Gerbeth, Marginal turbulent magnetohydrodynamic flow in a square duct, Phys. Fluids **22**, 084101 (2010).
[14] D. Krasnov, O. Zikanov, and T. Boeck, Numerical study of magnetohydrodynamic duct flow at high Reynolds and Hartmann numbers, J. Fluid Mech. **704**, 421 (2012).
[15] B. Knaepen and R. Moreau, Magnetohydrodynamic turbulence at low magnetic Reynolds numbers, Annu. Rev. Fluid Mech. **40**, 25 (2008).
[16] H. Kamkar and H. K. Moffatt, A dynamic runaway effect associated with flux expulsion in magnetohydrodynamic channel flow, J. Fluid Mech. **121**, 107 (1982).
[17] V. Bandaru, J. Pracht, T. Boeck, and J. Schumacher, Simulation of flux expulsion and associated dynamics in a two-dimensional magnetohydrodynamic channel flow, Theor. Comput. Fluid Dyn. **29**, 263 (2015).
[18] V. Bandaru, T. Boeck, D. Krasnov, and J. Schumacher, A hybrid finite difference-boundary element procedure for the simulation of turbulent MHD duct flow at finite magnetic Reynolds number, J. Comput. Phys. **304**, 320 (2016).
[19] A. B. Iskakov, S. Descombes, and E. Dormy, An integro-differential formulation for magnetic induction in bounded domains: Boundary element–finite volume method, J. Comput. Phys. **197**, 540 (2004).
[20] I. Stakgold, *Boundary Value Problems of Mathematical Physics* (SIAM, Philadelphia, 2000), Vol. 2.
[21] S. Tympel, T. Boeck, and J. Schumacher, Laminar and transitional liquid metal duct flow near a magnetic point dipole, J. Fluid Mech. **735**, 553 (2013).
[22] A. Iskakov and E. Dormy, On magnetic boundary conditions for non-spectral dynamo simulations, Geophys. Astrophy. Fluid Dyn. **99**, 481 (2005).
[23] U. Müller and L. Bühler, Liquid metal magneto-hydraulics flows in ducts and cavities, in *Magnetohydrodynamics: Lecture Notes of the 1999 Summer School Organised by IUTAM and HYDROMAG* (Springer, Berlin, 2002).
[24] U. Müller and L. Bühler, *Magnetohydrodynamics in Channels and Containers* (Springer, Berlin, 2001).
[25] A. Gailitis, O. Lielausis, E. Platacis, G. Gerbeth, and F. Stefani, Riga dynamo experiment and its theoretical background, Phys. Plasmas **11**, 2838 (2004).
[26] S. Kenjereš and K. Hanjalić, Numerical Simulation of a Turbulent Magnetic Dynamo, Phys. Rev. Lett. **98**, 104501 (2007).
[27] F. Krause and K.-H. Rädler, *Mean-Field Magnetohydrodynamics and Dynamo Theory* (Pergamon Press, New York, 1980).
[28] D. Krasnov, O. Zikanov, J. Schumacher, and T. Boeck, Magnetohydrodynamic turbulence in a channel with spanwise magnetic field, Phys. Fluids **20**, 095105 (2008).
[29] S. C. Kassinos, B. Knaepen, and A. Wray, Statistical measures of structural anisotropy in MHD turbulence subjected to mean shear and frame rotation, J. Turbul. **7**, N26 (2006).
[30] J. Jeong and F. Hussein, On the identification of a vortex, J. Fluid Mech. **285**, 69 (1995).
[31] Z. Warhaft, Turbulence in nature and the laboratory, Proc. Natl. Acad. Sci. USA **99**, 2481 (2002).
[32] J. Schumacher, K. R. Sreenivasan, and P. K. Yeung, Derivative moments in turbulent shear flows, Phys. Fluids **15**, 84 (2003).